International Journal of Heat and Mass Transfer 234 (2024) 126076

Contents lists available at ScienceDirect

International Journal of Heat and Mass Transfer

journal homepage: www.elsevier.com/locate/ijhmt

Three-dimensional cellular structures for viscous and thermal energy control in acoustic and thermoacoustic applications

Elio Di Giulio [a,*], Cong Truc Nguyen [b], Antonio Gloria [a], Camille Perrot [b], Raffaele Dragonetti [a]

[a] Department of Industrial Engineering, University of Naples Federico II, 80125 Naples, Italy
[b] Univ Gustave Eiffel, Univ Paris Est Creteil, CNRS, UMR 8208, MSME, F-77454 Marne-la-Vallée, France

ARTICLE INFO

Keywords:
Additive manufacturing
Cellular structure
Energy control
Transport parameters
Design methods

ABSTRACT

The multi-scale asymptotic method provides a separate description of the viscous and thermal response functions governing acoustic waves propagation through porous materials. However, these response functions are inherently interdependent for simple porous structures such as slits or tubes – their determination being directly influenced by the microstructural features of the geometry. This study aims to identify, characterize, and realize a microgeometry providing the ability to independently modify the viscous and thermal behaviours. A relative autonomy in the control of these phenomena would make it possible to regulate energy conversion processes within the structure, which can be either dissipative (e.g., sound absorption) or generative (e.g., thermoacoustic gain). Among the various microgeometries, cellular solids made by an assembly of cells with solid edges or faces, packed together so that they fill space, emerge as promising candidates for achieving such a goal. Within the interconnected cells (pores), the viscous losses are governed by the aperture sizes of the faces (throat section). On the other hand, the thermal exchanges are closely related to the interface between the fluid and the solid and consequently to the dimensions of the cells. The identified microstructure is a typical Kelvin cell-based geometry, modified to account for manufacturing constraints, and characterized by faces with well-defined opening ratio and thickness. This work presents a model, experimentally validated, to predict the transport parameters of such cellular solids. It provides a valuable tool for designing microstructures having the attributes to independently tune thermal and viscous effects for specific application requirements.

1. Introduction

The flow of fluids and diffusion of heat through porous media is important to a wide variety of environmental and technological processes. Practical examples of scientific and technological interest include the thermal management of battery pack [1], the modelling of sound absorbing materials [2], energy-conversion devices [3–5] and heat protective materials' spectral properties [6,7]. Lotton et al. [8] considered an accurate analytical solution including a precise quantification of heat transfer mechanisms in a stack of plates. Hariharan et al. [9] studied possible improvements of the performance by focusing either on operational, geometrical or fluid parameters. The geometrical parameters were limited to stack position, stack length and resonator length. Kuzuu and Hasegawa [10] performed both CFD simulation and numerical heat transfer analysis in a straight channel thermoacoustic to better understand the non-linear behaviour of the temperature field in a thermoacoustic engine core. In all case, a better understanding of the temperature and velocity fields is required to gain insight into the heat transfer mechanisms and improve the corresponding performance. We extend this work by considering more specifically the cellular design of the stack. Recently, there has been a great interest in understanding the relationship between the transport of fluids and diffusion of heat and the geometry of porous media [11–14]. Elementary transport processes can be used to probe the salient features of the pore structure [15–18], and vice versa [19–24]. Our aim in this paper is to propose a microstructure that can be used to promote thermal relaxation effects while maintaining viscous dissipation as small as possible in order to achieve a substantial fraction of Carnot's efficiency in thermoacoustic engines.

Controlling the geometrical features of porous material/structure enables the regulation of viscous and thermal phenomena inside the microstructure. In general, these two phenomena are strictly linked, because both the viscous and thermal processes inside a porous material are related to its own microstructure. As an illustration, simple geometries, such as uniform cross-sectional materials, exhibit interdependent viscous and thermal responses [25]. By changing the radius of a circular

* Corresponding author.
E-mail address: elio.digiulio@unina.it (E. Di Giulio).

https://doi.org/10.1016/j.ijheatmasstransfer.2024.126076
Received 1 March 2024; Received in revised form 5 April 2024; Accepted 13 August 2024
0017-9310/© 2024 The Author(s). Published by Elsevier Ltd. This is an open access article under the CC BY license (http://creativecommons.org/licenses/by/4.0/).

Nomenclature

A	Cross-sectional area $[m^2]$
c_p	Fluid specific heat at constant pressure $\left[\frac{J}{kg \cdot K}\right]$
d	Sample thickness $[m]$
D_t	Size of the unit cell $[m]$
$\boldsymbol{e}$	Unit vector $[-]$
f	Frequency $[H_z]$, thermoviscous functions $[-]$
i	Imaginary unit
$\widetilde{k}_n$	Complex wave number $[1/m]$
$\widetilde{k}$	Dynamic viscous permeability $[m^2]$
$\widetilde{k}'$	Dynamic thermal permeability $[m^2]$
$\widetilde{K}$	Complex bulk modulus $[Pa]$
k_0	Static viscous permeability $[m^2]$
k_0'	Static thermal permeability $[m^2]$
p	Acoustic pressure $[Pa]$
p_{up}	Acoustic pressure in the upper cavity $[Pa]$
p_{dw}	Acoustic pressure in the lower cavity $[Pa]$
T	Acoustic temperature $[K]$
t_0	Face opening ratio $[-]$
$\boldsymbol{v}$	Acoustic velocity $[m/s]$
V_{dw}	Lower cavity volume $[m^3]$
V_{up}	Upper cavity volume $[m^3]$
w	Scaled velocity vector $[-]$
x	Coordinate $[m]$
x_{mic}	Microphone's position $[m]$

Greek letters

α_∞	High frequency limit of tortuosity $[-]$
γ	Specific heat ratio $[-]$
δ	Viscous/thermal boundary layer $[m]$
θ	Microgeometrical parameter $[-]$
κ	Fluid thermal conductivity $\left[\frac{W}{m \cdot K}\right]$
Λ	Viscous characteristic length $[m]$
Λ'	Thermal characteristic length $[m]$
μ	Dynamic viscosity $[Pa{\cdot}s]$
ξ	Face thickness $[m]$
ρ	Acoustic density $[kg/m^3]$
$\widetilde{\rho}$	Acoustic complex density $[kg/m^3]$
τ	Scaled temperature $[-]$
φ	Porosity $[-]$
ϕ	Scalar potential $[-]$
ω	Angular frequency $[rad/s]$
Ω_f	Fluid Volume $[m^3]$
Ω	Total Volume $[m^3]$

Subscript

N	Viscous
K	Thermal
m	Mean time variable
s	Solid part
1	First order variable

pore, it is possible to modify both the thermal and the viscous contributions. In general, this also happens for classical acoustical materials like fibers, open-cell foams, granular.

However, in some cases, it may be important to govern the thermal or viscous effects independently. For example, in thermoacoustics, the core of such devices is a particular porous material, referred to as the stack. The aim is to enhance heat exchange between the oscillating fluid and its solid matrix while simultaneously reducing viscous losses.

The overall behaviour of porous materials is described through the dynamic viscous $k(\omega)$ and thermal $k'(\omega)$ permeability, which are two frequency-dependent complex parameters [13,26]. These parameters enable the characterization of the visco-thermal interaction between the solid skeleton and the oscillating fluid. We emphasize, following Johnson et al. [11] and Lafarge et al. [12], that $\widetilde{k}(\omega)$ and $\widetilde{k}'(\omega)$ depend on the tortuosity α_∞, the viscous Λ and thermal Λ' characteristic lengths of the pore space, the static viscous k_0 and thermal $k_0{}'$ permeabilities and the porosity φ. Accordingly, any estimate of $\widetilde{k}(\omega)$ and $\widetilde{k}'(\omega)$ must involve an estimate of the intrinsic macroscopic transport parameters (φ, k_0, $k_0{}'$, Λ, Λ', α_∞) relevant to fluid flow and heat transfer.

In the present paper, our aim is to examine a specific class of ordered three-dimensional cellular system and, for a large range of geometrical parameters, to compute the corresponding transport parameters (φ, k_0, $k_0{}'$, Λ, Λ', α_∞). By doing so, we hope to test the idea that tuning the cell size and the aperture ratio of a cellular structure can provide a valuable alternative to conventional thermoacoustic stacks. It is noteworthy that the viscous behaviour of such porous materials is closely linked to the throat section area and, consequently, to the membrane holes. On the other hand, the thermal behaviour depends on the solid-fluid interface and, therefore, the cell dimension.

Hence, the model cellular structure employed in our study is presented in Sec. 2, resulting as a promising candidate for realizing a porous structure where viscous and thermal behaviour can be independently tuned. In Sec. 3, we summarize the basic equations used for modelling visco-thermal properties in a porous material. In Sec. 4, correlation functions are used to quantitatively link pore structure with transport properties. In Sec. 5, we analyse the application of the correlation functions on the specific example of the thermal relaxation θ_κ and viscous dissipation θ_ν functions, which are closely linked to $\widetilde{k}(\omega)$ and $\widetilde{k}'(\omega)$. The design and the manufacturing process of the samples is reported in Sec. 6. In Sec. 7, our findings are compared with experimental data and discussed. The main findings are summarized in the Sec. 8.

2. Three-dimensional cellular structure

Recent developments in additive manufacturing technology (AM) allow to realize porous material/structure with tailored geometrical features as well as mechanical and mass transport properties [27–31]. Furthermore, AM technology imposes geometrical constraints that depends on the adopted manufacturing process. An open-celled foam micro-structural model is defined using a tetrakaidecahedron (Kelvin model) as a repeated unit-cell (Fig. 1). To account for the need of structural support imposed by the additive manufacturing process, the cell walls possess a thickness ξ. The properties of the porous structure are written as a function of the cell size of diameter D_t and the opening ratio of the faces $t_0 = \sqrt{A_o/A}$, where A_o denotes the opened surface area of the faces of surface area A. Simulations were performed in the range $0.2 \leq t_0 \leq 0.7$ and $0.003 \leq \xi/D_t \leq 0.2$ (in agreement with the constraints imposed by the manufacturing process, Sec. 5). Furthermore, due to the symmetry of the microstructure, one can easily recognize that the numerical computations can be carried out on one-eighth of the tetrakaidecahedron shown in Fig. 1.

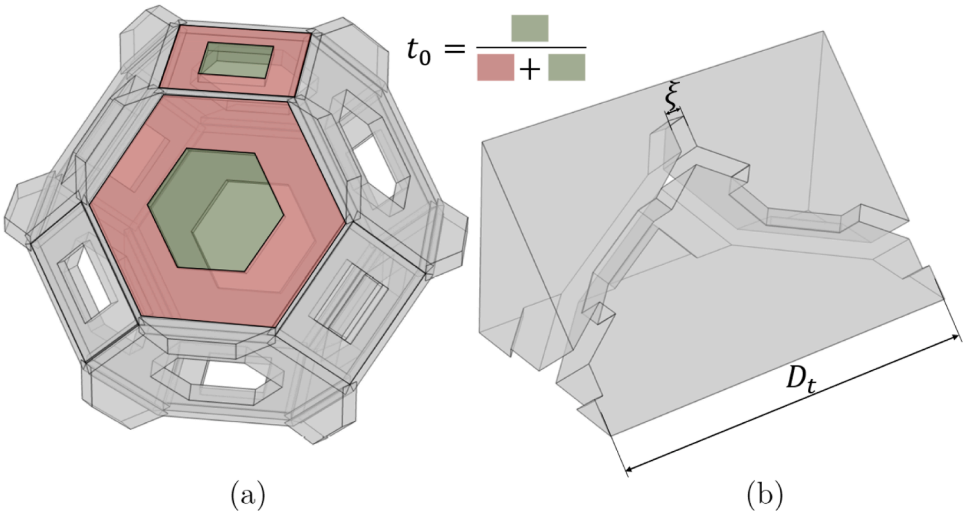

Fig. 1. Tetrakaidecahedron repeating unit cell illustrating the open-cell structure used in this study [left panel, (a)], together with one-eighth of the unit cell allowing to reduce the cost of the numerical calculations [right panel (b)].

3. Modeling visco-thermal properties

Consider a fluid-filled porous material with bicontinuous solid and fluid networks under the excitation of an external harmonic source with angular frequency $\omega = 2\pi f$ (f is the frequency). In the framework of linearized acoustics, air being considered as an ideal gas, the air motion inside the porous material is completely characterized, at the microscopic level, by the values of the acoustic velocity $\boldsymbol{v}$, the excess pressure p, the excess density ρ, and the excess temperature T fields. These variables obey the coupled equations of continuity, momentum, energy and the equation of state in the fluid domain Ω_f. In harmonic regime, this coupled visco-thermal problem can be written as:

$$\mu\left(\nabla^2\boldsymbol{v} + \frac{1}{3}\nabla(\nabla\cdot\boldsymbol{v})\right) - \nabla p = i\omega\rho_m\boldsymbol{v}, \tag{1}$$

$$\rho_m\nabla\cdot\boldsymbol{v} + i\omega\rho = 0, \tag{2}$$

$$\kappa\nabla^2 T = i\omega\rho_m c_p T - i\omega p, \tag{3}$$

$$\frac{p}{p_m} = \frac{\rho}{\rho_m} + \frac{T}{T_m}. \tag{4}$$

In the above equations, i with $i^2 = -1$ is the imaginary unit. The physical parameters of the saturating fluid are the dynamic density μ, thermal conductivity κ, heat capacity c_p. At the ambient conditions of pressure p_m and of temperature T_m, the density of the fluid is ρ_m. In this treatment, the solid frame displacement may be regarded as motionless. At the interface between the fluid and solid frame $\partial\Omega_f$, the no-slip $\boldsymbol{v} = 0$ and thermostat $T = 0$ conditions apply. The isothermal condition ($T = 0$) is justified owing to a much larger thermal capacity of the solid matrix with respect to the fluid one [32].

One may identify a scale separation between a small scale l that is given by the typical pore size D_t and a large scale L that is on the order of the wavelength λ of the incident sound wave ($L \sim \lambda/2\pi$). Under this scale separation, $\epsilon = l/L \ll 1$, the interplay between the viscous and thermal effects can be neglected at a first approximation [13]. With the existence of this scale separation, homogenization theory enables considering the periodic unit-cell (Fig. 1a) as a Representative Elementary Volume (REV) and provides theoretical evidence supporting the following semi-phenomenological relationships for the dynamic viscous $\widetilde{k}$ (Johnson et al.) and thermal $\widetilde{k}'$ (Lafarge et al.) permeabilities defined by a generalized Darcy's law and its thermal counterpart:

$$\varphi\langle\boldsymbol{v}\rangle = -\frac{\widetilde{k}(\omega)}{\mu}\nabla\langle p\rangle, \tag{5}$$

$$\varphi\langle T\rangle = \frac{\widetilde{k}'(\omega)}{\kappa} i\omega\langle p\rangle, \tag{6}$$

where $\langle\cdot\rangle$ defines averaging,

$$\langle\cdot\rangle = \frac{1}{\Omega}\int_{\Omega_f}(\cdot)\, d\Omega. \tag{7}$$

The porosity φ is defined as the ratio between Ω_f, the volume occupied by the filling fluid, and Ω, the total volume of the unit-cell: $\varphi = \Omega_f/\Omega$. $\widetilde{k}$ and $\widetilde{k}'$ are two frequency-dependent response functions used to describe sound propagation at the macroscopic level. In the limit of low frequencies ($\omega \to 0$), the real constants $k_0 = \lim_{\omega\to 0}\widetilde{k}(\omega)$ and $k_0' = \lim_{\omega\to 0}\widetilde{k}'(\omega)$ play the role of the static viscous and thermal permeabilities. In the limit of high frequencies, the asymptotic expressions for $\widetilde{k}(\omega)$ and $\widetilde{k}'(\omega)$ can be deduced from the knowledge of the viscous Λ and thermal Λ' characteristic lengths, together with the high frequency limit of the tortuosity α_∞. The set of these parameters(φ, k_0, k_0', Λ, Λ', α_∞) represent the six geometrical and transport parameters used as inputs into the analytical formulation for the complex density $\widetilde{\rho}$ and bulk modulus $\widetilde{K}$ of the porous material, as defined by Johnson-Champoux-Allard-Lafarge (JCAL) semi-phenomenological model (see Appendix A). The link between the dynamic permeabilities $[\widetilde{k}(\omega), \widetilde{k}'(\omega)]$ and the complex density and bulk modulus $[\widetilde{\rho}, \widetilde{K}]$ can be written as:

$$\widetilde{k} = \frac{\delta_\nu^2}{2i}\frac{\rho_m}{\widetilde{\rho}}, \tag{8}$$

$$\widetilde{k}' = \frac{\delta_\kappa^2}{2i}\frac{\gamma}{\gamma - 1}\left(1 - \frac{p_m}{\widetilde{K}}\right). \tag{9}$$

Here, γ is the specific heat ratio, while $\delta_\nu = \sqrt{2\mu/\omega\rho_m}$ and $\delta_\nu = \sqrt{2\kappa/\omega\rho_m c_p}$ are respectively the viscous and thermal boundary layers. The derivation of these equalities [Eqs. (8)-(9)] is reported throughout Appendix B.

The transport parameters of a porous media are determined on the three-dimensional periodic unit-cell using a finite element method for solving three boundary value problems in the pore space (Fig. 1 and Fig. 2) [33–35].

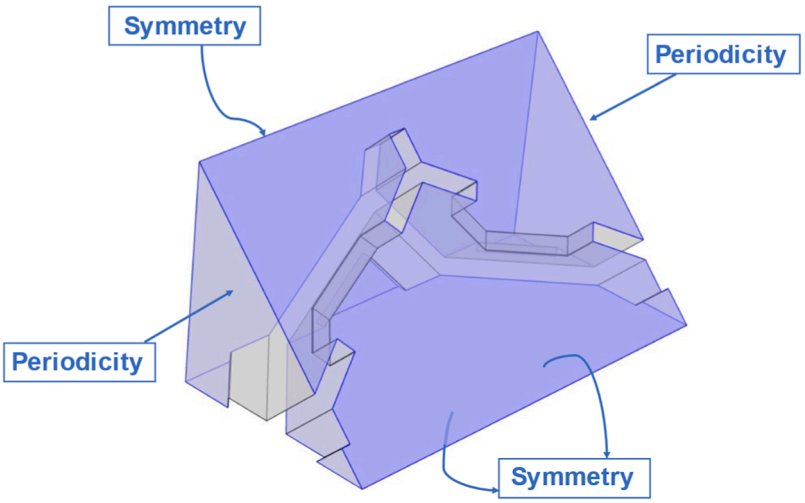

Fig. 2. Boundary conditions applied to solve the boundary value problems of interest.

1. Scaled Stokes' problem

The static viscous permeability k_0 can be obtained from a scaled Stokes' problem with two Ω-periodic unknowns $\boldsymbol{w}$ (vector field) and π (scalar field) [33]:

$$-\nabla^2 w + \nabla\pi = e, \ in\ \Omega_f, \tag{10}$$

$$\nabla\cdot w = 0, \ in\ \Omega_f, \tag{11}$$

$$w = 0, \ on\ \partial\Omega_f. \tag{12}$$

where $\boldsymbol{e}$ is a constant unit vector of the direction in which the flow is globally driven. The static viscous permeability k_0 for the preferential flow direction $\boldsymbol{e}$ is computed as follows:

$$k_0 = \varphi\langle \boldsymbol{w}\cdot\boldsymbol{e}\rangle. \tag{13}$$

2. Laplace's problem

In the high frequency range, the viscous boundary layer becomes negligible, and the fluid behaves as an inviscid perfect one. According to the works of Johnson et al. [11], Brown [36], and Avellaneda and Torquato [37], this problem is equivalent to a boundary value problem of electric conduction, where the conducting fluid having a constant conductivity fills the porous media. Laplace's problem for the scalar Ω-periodic unknown ϕ can be written, together with the boundary conditions, as

$$\nabla^2\phi = 0 \ in\ \Omega_f, \tag{14}$$

$$\nabla\phi\cdot n = e\cdot n \ on\ \partial\Omega_f, \tag{15}$$

with $\boldsymbol{E} = \boldsymbol{e} - \nabla\phi$ and ϕ are respectively the local electric fields and a scalar potential. Therefore, the high frequency limit of the tortuosity, α_∞, and the viscous characteristic length, Λ, can be evaluated as

$$\alpha_\infty = \frac{\langle \boldsymbol{E}\cdot\boldsymbol{E}\rangle}{\langle \boldsymbol{E}\rangle\cdot\langle \boldsymbol{E}\rangle}, \tag{16}$$

$$\Lambda = 2\frac{\int_{\Omega_f}\boldsymbol{E}\cdot\boldsymbol{E}d\Omega}{\int_{\partial\Omega}\boldsymbol{E}\cdot\boldsymbol{E}dS}. \tag{17}$$

3. Poisson's problem

The static thermal permeability k_0' is evaluated from a diffusion-controlled process. Lafarge et al. [12] pointed out the link between the acoustic fluctuations of temperature and the time derivative of acoustic pressure, Eq. (6). The static thermal permeability is useful to describe these thermal effects in the fluid saturating a solid skeleton, which can be considered as a thermostat. Furthermore, the Poisson's problem for the scalar Ω-periodic unknown τ is written as:

$$\nabla^2\tau = -1 \ in\ \Omega_f\ , \tag{18}$$

$$\tau = 0 \ on\ \partial\Omega. \tag{19}$$

Using the solution field of this boundary value problem, static thermal permeability k_0' is estimated as $k_0' = \varphi\langle\tau\rangle$.

Porosity and thermal characteristic length are purely geometrical transport parameters not related to a specific physical field. Their values can be assessed simply by using their definitions, as

$$\varphi = \frac{\Omega_f}{\Omega}, \tag{20}$$

$$\Lambda' = 2\frac{\int_{\Omega_f} d\Omega}{\int_{\partial\Omega} dS}. \tag{21}$$

It should be noted that due to the symmetry of the periodic unit-cell, it is possible to utilize only one-eighth of the structure, effectively reducing the computational expenses involved in the determination of the solution fields. In this case, the symmetry conditions are used to replace the periodic conditions on the cut-off boundaries while in the preferential direction of flow, the periodic conditions are always maintained (Fig. 2). More specifically, the condition set on each symmetric face is: $\boldsymbol{w}\cdot\boldsymbol{n} = 0$ for the scaled Stokes' problem; $\boldsymbol{E}\cdot\boldsymbol{n} = 0$ for the Laplace's problem; $\nabla\tau\cdot\boldsymbol{n} = 0$ for the Poisson's problem (Fig. 2).

An example of three solution fields (microscopic velocity, electric potential and scaled temperature) within the fluid phase of the open-celled foam micro-structural model under study is reported in Fig. 3. It is worth noting how the fluid velocity increases in the vicinity of the wall apertures (Fig. 3a). The same regions have also great influence on the values of the electric field (Fig. 3b). These areas correspond to the domain where the viscous losses occur, and greatly influence the values of the viscous permeability k_0, tortuosity α_∞, and viscous characteristic length Λ [Eqs. (16)-(17)]. On the other hand, Fig. 3c highlights the contribution of the fluid volume within the cells away from the fluid-solid interface $\partial\Omega$ in determining the thermal behaviour of the structure. To ensure a numerical convergence in the computation of $\boldsymbol{E}\cdot\boldsymbol{E}$ [Eqs. (16)-(17)] the sharp edges were replaced by small smooth fillets with radius (R_F = 0.001 mm) much smaller than the radii of pores and

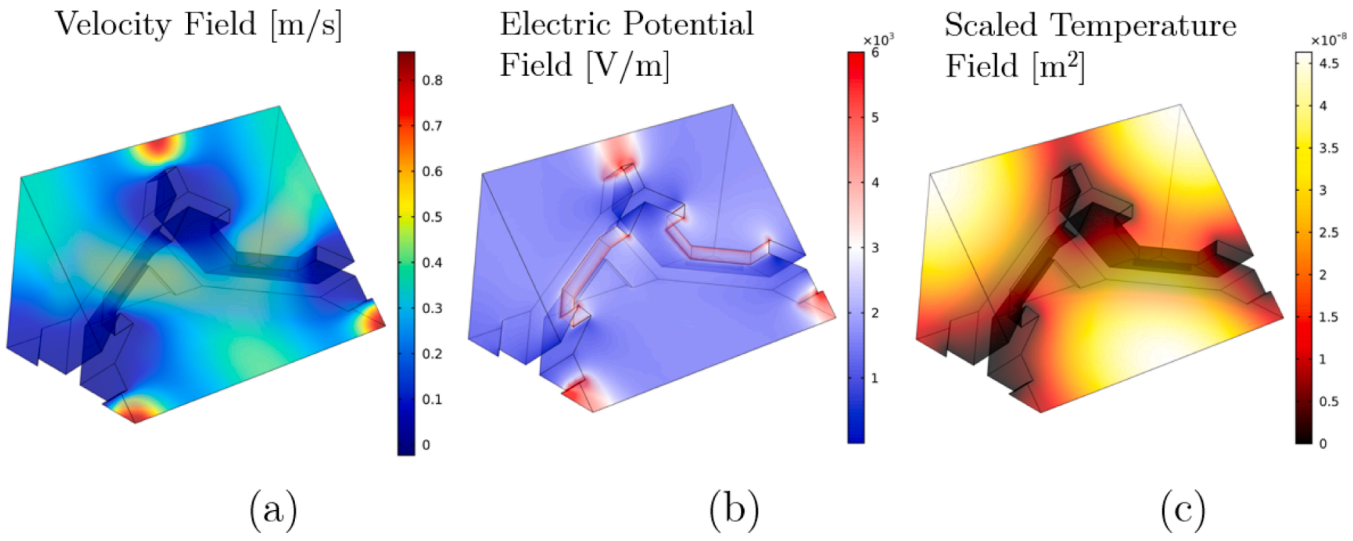

Fig. 3. Fields of (a) the scaled velocity $\boldsymbol{w}$ under the application of a macroscopic driving force e; (b) the electric potential ϕ corresponding to a unit differential stimulus $\boldsymbol{e}$, and (c) the scaled temperature field $\boldsymbol{\tau}$.

windows [38].

4. Correlations between pore structure and transport properties

Certain porous media with rather simple geometries such as the one studied in this paper allow analytical calculations of the porosity φ and thermal characteristic length Λ'. In the limit of thin walls, $\xi \to 0$, the solid volume at the intersection between faces can be ignored so that the proposed analytical relationships between the geometric parameters (φ, Λ') and the microstructural descriptors (D_t, ξ, t_0) hold almost exactly.

Doutres et al. [39] proposed empirical power laws in $1/R_w$ for α_∞, where R_w is defined by the closed pore content of a foam. We then extend this power law in $1/t_0$ for α_∞ on our periodic unit cell so as to also include the $1/\varphi$ porosity dependency. Similarly, the ratio of thermal over viscous characteristic lengths Λ'/Λ is no more constant, when the opening ratio t_0 is decreasing, and also depends on porosity φ. This is clearly seen in the power law for Λ'/Λ in $1/t_0$ and φ. The dimensionless permeability k_0/D_t^2, was related analytically to d_0^3 where d_0 is the aperture size (Sampson's law) [40,41]. The prediction for k_0/D_t^2 could then be extended to $c'\varphi t_0{}^3$, where c' is an unknown, but hopefully calculable, constant scale factor. The dimensionless static thermal permeability k_0'/D_t^2 was analytically related to $-\ln(1-\varphi)$ for fibrous media [40], and therefore found to diverge when $\varphi \to 1$. Finite element computations performed by Hoang and Perrot [42] also shown analogue results for cellular structures with thin membranes when $t_0 \to 0$. Furthermore, the inequality $k_0'/D_t^2 \geq k_0/D_t^2$ holds for all φ [37]. All of these results are consistent with the fit obtained with our data, stating that the thermal permeability is proportional to the product of power laws in φ and t_0 for the open-celled cellular structure in situations departing from $\xi/D_t \to 0$. All the correlations functions that relate the dimensionless macroscopic properties (φ, Λ'/D_t, Λ'/Λ, α_∞, k_0/D_t^2, k_0'/D_t^2) to pore-structure (t_0, ξ/D_t) parameters are summarized in Table 1. A distinction can then be made between dimensionless visco-inertial (k_0/D_t^2, α_∞, Λ/D_t) and thermal (k_0'/D_t^2, Λ'/D_t) parameters when plotting them with the porosity φ against the opening ratio t_0 and the dimensionless wall thickness ξ/D_t (Fig. 4). It is clearly seen that the walls opening ratio t_0 is the pore-structure parameter that mostly determine the material's visco-inertial (Fig. 4.a, 4.c, 4.e) and thermal (Fig. 4.b, 4.d, 4.f) properties, compared to the wall thickness ξ/D_t. It is also of interest to mention that the wall thickness ξ/D_t is comparatively more influent on the thermal parameters than on the visco-inertial ones (Fig. 1). However, in the studied range of parameters, $0.2 \leq t_0 \leq 0.7$ and $0.003 \leq \xi/D_t \leq 0.2$, it turns out that the effect of the wall thickness ξ/D_t is small on thermal characteristic length Λ'/D_t and permeability k_0'/D_t^2, so that these parameters tend to be relatively non-sensitive to the wall thickness ξ/D_t values.

Table 1
Transport parameters' correlations for the open-celled foam micro-structural model shown in Fig. 1, considering a wall of thickness ξ/D_t which can be chosen to make the structure manufacturable. R-squared is the coefficient of determination, while SSE denotes the sum squared errors of residuals.

Correlation	R-Squared	SSE
$\varphi = 1 - \frac{9}{16}\left(1+2\sqrt{3}\right)\left(1-t_0^2\right)\frac{\xi}{D_t}$	0.9875	0.01649
$\frac{\Lambda'}{D_t} = \frac{2\varphi}{6\left(1-t_0^2\right)+\frac{\xi}{D_t}}$	0.9534	0.03528
$\frac{\Lambda'}{\Lambda} = (\varphi)^{0.2468}\left(\frac{1}{t_0}\right)^{0.9609}$	0.9556	3.254
$\alpha_\infty = 0.6668(\varphi)^{-0.4703}\left(\frac{1}{t_0}\right)^{0.9678}$	0.9641	1.984
$\frac{k_0}{D_t^2} = 0.03249\varphi t_0^3$	0.9974	2.334e-6
$\frac{k_0'}{D_t^2} = 0.04023\varphi^{3.265}t_0^{2.494} + 0.01097\left(\frac{\xi}{D_t}\right)^{-0.07873}$	0.9778	4.506e-5

5. Tuning thermal and viscous exchanges

Sec. 3 gives an explicit recipe for the numerical calculation of the viscous $\tilde{k}$ and thermal $\tilde{k}'$ response functions from the knowledge of the microstructure parametrized by the cell diameter D_t, the wall thickness ξ and the aperture ratio t_0. However, there was still a need, in particular for open-celled cellular structures that can be obtained using additive manufacturing, for simple and compact analytical models that enable the viscous and thermal exchanges of these porous materials to be understood on the basis of microstructural parameters. For that purpose, we carried out systematic calculations in Sec. 4 to provide direct relations between the macroscopic transport parameters (φ, k_0, k_0', Λ, Λ', α_∞) and the microstructure coefficients D_t, ξ/D_t and t_0 (Table 1 and Fig. 4). This micro-structural model employed a Kelvin-like model geometry (Sec. 2) which is adapted to account for some constraints induced by additive manufacturing, by taking into account not only the size D_t and opening ratio t_0 of the repeating unit cell, but also the corresponding wall thickness ξ. The effect of these size parameters on the

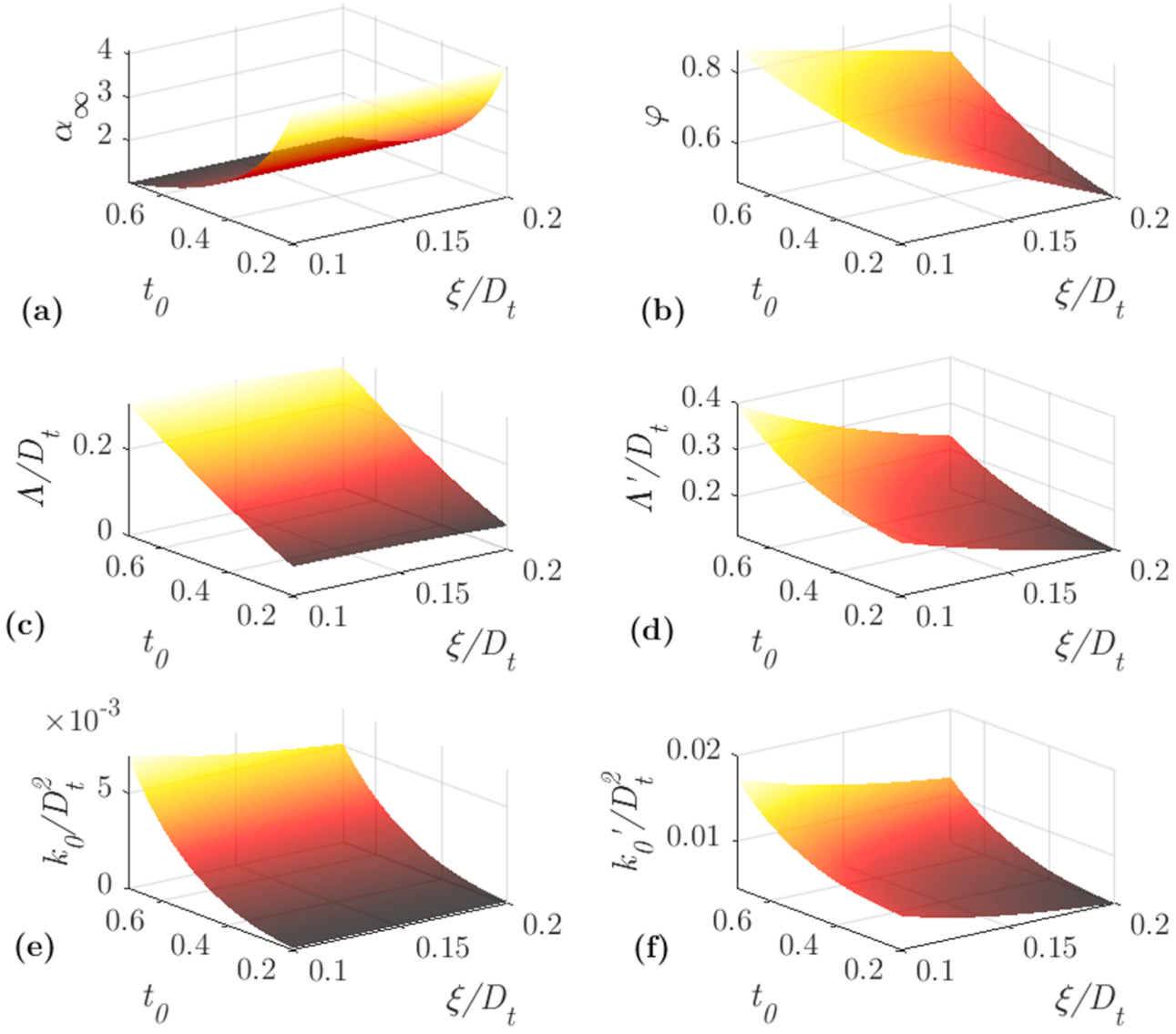

Fig. 4. Dimensionless transport parameters versus wall thickness $\boldsymbol{\xi/D_t}$ and aperture ratio $\boldsymbol{t_0}$. On the left column, the visco-inertial parameters: (a) the high frequency limit of the tortuosity $\boldsymbol{\alpha_\infty}$, (c) the dimensionless viscous characteristic length $\boldsymbol{\Lambda/D_t}$, (e) the dimensionless static viscous permeability $\boldsymbol{k_0/D_t^2}$. On the right column, the porosity and thermal parameters: (b) the porosity $\boldsymbol{\varphi}$, (d) the dimensionless thermal characteristic length $\boldsymbol{\Lambda'/D_t}$, (f) the dimensionless static thermal permeability $\boldsymbol{k_0'/D_t^2}$.

thermal and viscous exchanges is demonstrated in this section, and the advantages of this more general micro-structural model for thermo-acoustic applications are illustrated. To derive the associated viscous and thermal frequency-dependent terms, we followed closely Swift [3] (Sec. 5.1.1, Eq. 5.10) for acoustic power dissipation without "carrying heat" from a temperature gradient inside the stack (porous material), which led us to the following dimensionless viscous dissipation θ_ν and thermal-relaxation θ_κ functions (see Appendix B):

$$\theta_\nu = \delta_\nu^2 \frac{\Re[\widetilde{k}]}{|\widetilde{k}|^2}, \quad (22)$$

$$\theta_\kappa = \frac{2}{\delta_\kappa^2} R[\widetilde{k}]. \quad (23)$$

Here, $\Re$ denotes the real part of a complex number. The latter dimensionless functions θ_ν and θ_κ are important to build understanding, through a quantitative discussion. Indeed, the viscous losses and the thermal relaxation processes inside a porous material may either contribute to an energy dissipation or to a thermoacoustic energetic gain.

The effect of the value of the opening ratio t_0 of the walls of the unit cell is illustrated in Fig. 5, where the other parameters of the tetrakaidecahedron, the unit cell diameter D_t and the wall thickness ξ, are kept to the same values ($D_t = 2$ mm, $\xi/D_t = 0.1$). Increasing the opening ratio t_0 by a factor of 2.4 significantly decreases the viscous dissipation factor θ_ν of about tenfold. On the other hand, increasing the opening ratio t_0 by a factor of 2.4 has a relatively little effect on the thermal-relaxation factor θ_κ. The thermal-relaxation factor θ_κ increased by a factor of about 1.2 in the vicinity of the thermal transition frequency $f_{\kappa t} = \kappa\varphi/2\pi\rho_m c_p k_0'$, where both isothermal and adiabatic regimes coexist. Importantly, we therefore note that increasing the opening ratio t_0 is therefore a mean for reducing viscous dissipation (loss in acoustic power) while maintaining the thermal exchanges to a similar order of magnitude.

The effect of wall thickness ξ is documented in Fig. 6, in which the viscous dissipation θ_ν and thermal-relaxation θ_κ functions are displayed for different values of this parameter, namely 100, 200 and 360 μm. The

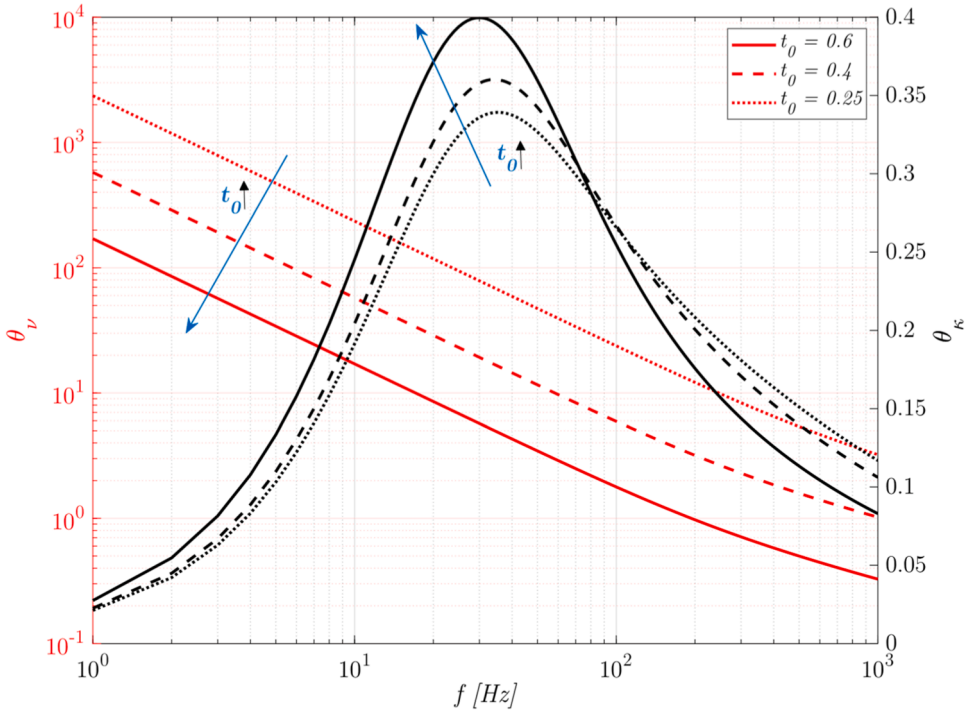

Fig. 5. Viscous dissipation $\boldsymbol{\theta_\nu}$ (left y-axis) and thermal-relaxation $\boldsymbol{\theta_k}$ (right y-axis) functions versus frequency for three different aperture ratio $\boldsymbol{t_0}$, as shown in the legend of the plot on the right, at constant dimensionless wall thickness $\boldsymbol{\xi/D_t}$ of 0.1 and cell size $\boldsymbol{D_t}$ equal to 2 mm.

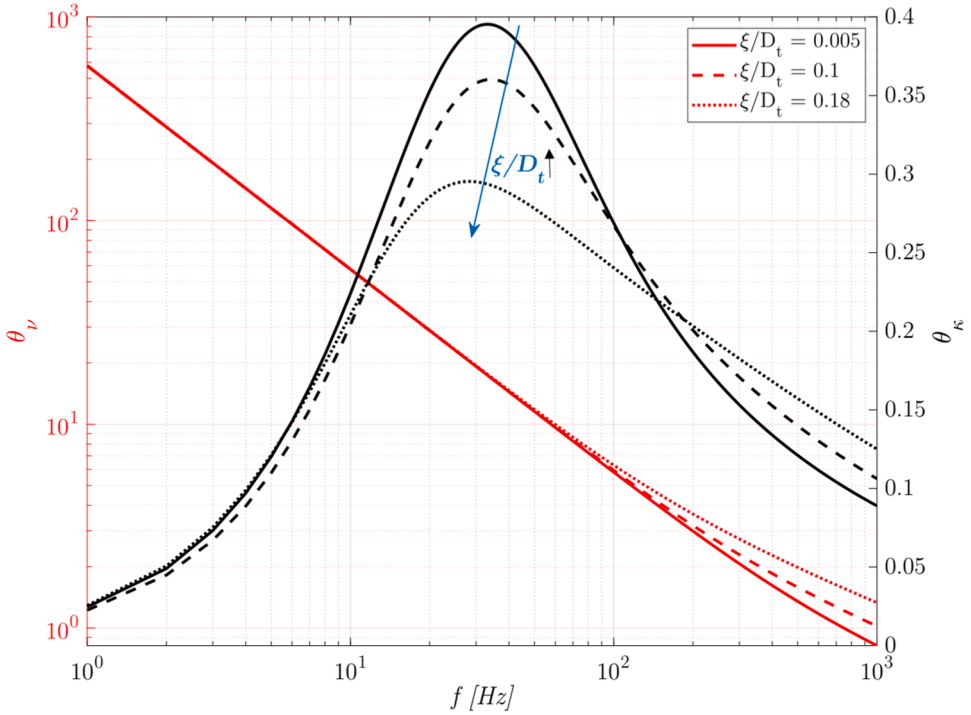

Fig. 6. Viscous dissipation θ_ν (left y-axis) and thermal-relaxation θ_κ (right y-axis) functions versus frequency for three different dimensionless wall thickness ξ /D_t, as shown in the legend of the plot on the right, at constant opening ratio t_0 of 0.4 and cell size D_t equal to 2 mm.

influence of wall thickness was quantitatively small on the viscous dissipation θ_ν, presumably because visco-inertial effects are dominated by the opening ratio t_0 and to a lesser content by porosity (see Table 1, d-e and a). Around the thermal transition frequency $f_{\kappa t}$, lowering the wall thickness ξ slightly increases the thermal-relaxation factor θ_κ by a factor of about 1.35. The results from this study suggest that it is preferable to avoid too thick walls when manufacturing the corresponding unit cells.

Finally, we note that the plot of the viscous dissipation θ_ν and thermal-relaxation θ_κ functions versus frequency for three different cell diameters D_t (D_t = 2, 3 and 4 mm) using constant opening ratio t_0 in-

dicates that increasing the cell size (by a factor of two) both decreases the viscous dissipation θ_ν (by a factor of two) and shifts the maximal thermal-relaxation coefficient θ_κ to lower frequencies (by a factor of about 2.4) – at constant relaxation coefficient θ_κ; Fig. 7. Because the cell sizes are increased at constant opening ratio t_0, the aperture radii are proportional to the cell size D_t, which leads to the observed viscous dissipation θ_ν drop. In contrast, when ξ/D_t and t_0 are fixed to given values, the ratio Λ'/D_t is expected to be a constant (Table 1) and the corresponding variation in the amplitude of θ_κ to be negligible. In the case of constant opening ratio t_0, the larger the pore size D_t, the lower the viscous dissipation θ_ν, but we get as a consequence that the frequency at which the maximal thermal-relaxation coefficient θ_κ occurs is also lowered.

6. Design and manufacturing of samples

The tetrakaidecahedron (Kelvin cell) models (Sec. 2, Fig. 1) are generated using a Computer-Aided Design (CAD) software (PTC Creo) with D_t, ξ and t_o as input geometrical parameters. The corresponding elementary periodic volume is translated and combined with Boolean operations to convert the solid skeleton into a cylindrical sample. Three samples are printed using $D_t = 8$ *mm*, $\xi = 0.8$ *mm* and $t_o = 0.25$ for sample 1 (S1), $t_o = 0.4$ for sample 2 (S2) and $t_o = 0.6$ for sample 3 (S3). The diameter of the samples is 100 *mm*, and the thickness is equal to 60 *mm*. The representative unit cells and the corresponding cylindrical samples are shown in Fig. 8. The CAD software is also used to generate the files providing the instructions to the printer.

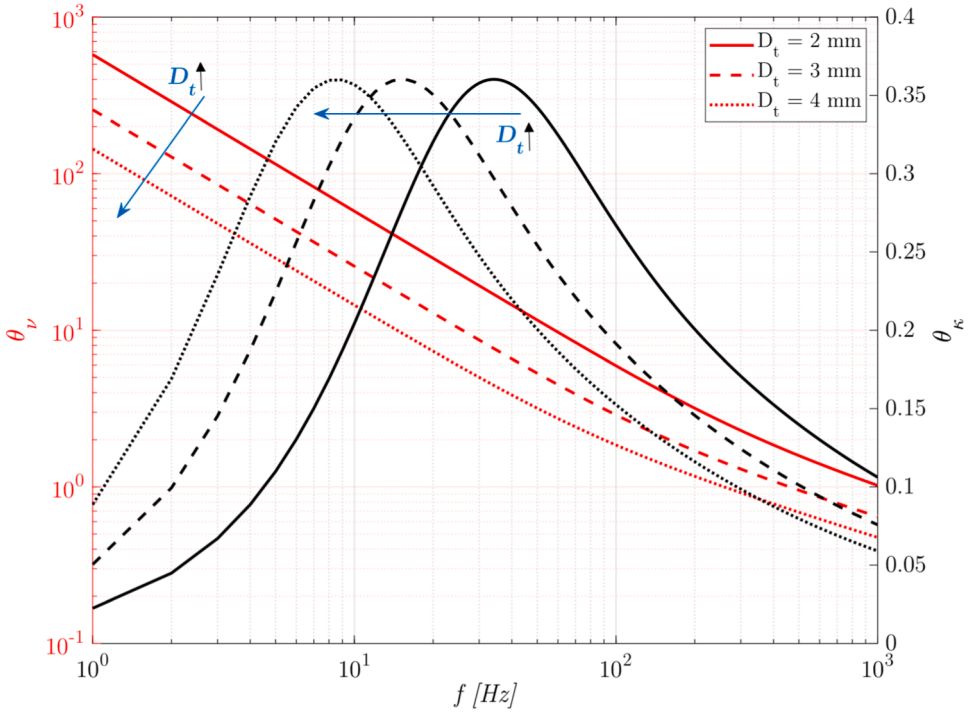

Fig. 7. Viscous dissipation θ_v (left y-axis) and thermal-relaxation θ_κ (right y-axis) functions versus frequency for three different cell sizes D_t, as shown in the legend of the plot on the right, at constant opening ratio t_0 of 0.4 and dimensionless wall thickness ξ/D_t equal to 0.1.

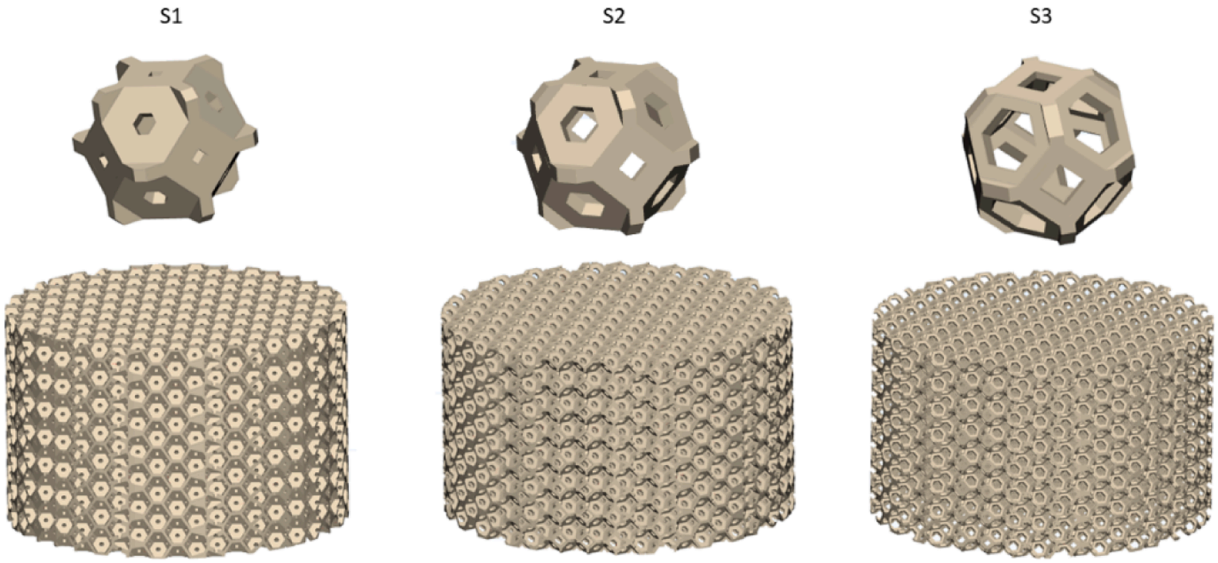

Fig. 8. Geometric models of 3D membrane structures obtained using the three unit cells marked as S1, S2 and S3.

Table 2
List of AM process parameters - held factors.

Factor	Value
Process/Printing Temperature (°C)	210
Layer Height (μm)	200
Bed Temperature (°C)	60
Printing Speed (mm/s)	45

An image of the 3D printed samples is reported in Fig. 9.

The Fusel Deposition Modelling (FDM) Prusa i3 MK3 printer is used to produce samples (with a diameter of 100 *mm* and a thickness of 60 *mm*). The extruded material is polylactic acid (PLA). The diameter of the nozzle is $d_n = 400\ \mu m$. The revolution axis of the sample is placed vertically. The nozzle temperature is set to 210^oC. The printing speed is 45 mm/s, and Table 2 reports the employed process parameters.

The printer nozzle extrudes a layer of rods in the horizontal plane, then the build plate shifts vertically and allows the next layer to be printed. The build plate displacement is set to 200 μm.

7. Experimental results and discussion

In order to characterize the viscous $\widetilde{k}$ and thermal $\widetilde{k}'$ response functions of the manufactured samples, we have used an experimental setup previously developed to improve the accuracy of the measurements in the low frequency range [43,44]. The technique relies on the lumped element approach. Figs. 11 and10 show the experimental setup used to characterize the dynamic viscous $\widetilde{k}$ function and the dynamic thermal $\widetilde{k}'$ function, respectively. The measurement procedure relies on two distinct acquisitions for each response function: one measurement where the sample is filling the cavity downward the loudspeaker (full, left panel) and one measurement end without the sample (empty, right panel). The "empty" tests correspond to a correction accounting for imperfect rigid backing or for the effect of radiation impedance with the open termination. By leveraging different boundary conditions (open termination or rigid backing) and measuring the acoustic pressure field in both the lower cavity p_{dw} and the upper cavity p_{up}, it is possible to provide an experimental estimate of the dynamic mass density $\widetilde{\rho}$ and the dynamic bulk modulus $\widetilde{K}$ of the manufactured samples, as:

$$\widetilde{\rho} = \varphi\left(\rho_m + \frac{\gamma p_m A}{\omega^2 V_{dw}(d - x_{mic})}\left[\left(\frac{p_{up}}{p_{dw}}\right)_{full} - \left(\frac{p_{up}}{p_{dw}}\right)_{empty}\right]\right), \tag{24}$$

$$\widetilde{K} = \frac{\gamma p_m}{\frac{1}{\varphi} - \frac{V_{dw}}{V_{up}\varphi}\left[\left(\frac{p_{up}}{p_{dw}}\right)_{full} - \left(\frac{p_{up}}{p_{dw}}\right)_{empty}\right]}, \tag{25}$$

where d and A are respectively the thickness and the cross-sectional area of the sample, x_{mic} is the microphone's position (relevant for the complex density measurement); V_{dw} and V_{up} are the lower and upper cavity volume. This method is limited to the low frequency range and must satisfy $|\widetilde{k}_n d| < 0.5$ where $\widetilde{k}_n = \omega\sqrt{\frac{\widetilde{\rho}}{\widetilde{K}}}$ is the complex wavenumber of the compressional wave propagating inside the sample. Once $\widetilde{\rho}$ and $\widetilde{K}$ are known, similar frequency-dependent response functions can be obtained; like $\widetilde{k}$ and $\widetilde{k}'$, f_ν and f_κ or θ_ν and θ_κ (Appendix B).

7.1. Comparison with experimental results

In Figs. 13, 14 and 15, the real and imaginary parts of the viscous $\widetilde{k}$ and thermal $\widetilde{k}'$ permeabilities are plotted versus the frequency in order to compare both modelled and measured data for the three manufactured samples S1, S2 and S3, respectively. More details on the assessment of the measurement uncertainties are reported in Supplementary Material. These figures suggest the following comments: (*i*) as expected, the modelled and measured data are generally in good agreement; (*ii*) the dispersion of the experimental results increases with decreasing frequency. These dispersions of the experimental data in the lower frequency range are attributed to the acoustic source, which was not specifically designed to operate in the low frequency range (like a woofer). A better appreciation of the behaviour of the dynamic viscous $\widetilde{k}$ and thermal $\widetilde{k}'$ permeabilities can be obtained by an approximate calculation of the viscous $f_{\nu t} = \mu\varphi/2\pi\rho_m\alpha_\infty k_0$ and thermal $f_{\kappa t} = \kappa\varphi/2\pi\rho_m c_p k_0'$ transition frequencies equal to 3 *Hz* and 25 *Hz* for S1, 3 *Hz* and 10 *Hz* for S2, 2 *Hz* and 4 *Hz* for S3, respectively. These values reveal that the observed frequency-dependent properties essentially correspond to their high frequency behaviour. This is not surprising because the viscous $f_{\nu t}$ and thermal $f_{\kappa t}$ transition frequencies are primarily governed by their respective viscous k_0 and thermal k_0' static permeabilities that are related to the square of the cell size D_t ($k_0 \sim D_t^2$, $k_0' \sim D_t^2$) and are drastically increasing with the opening ratio ($\frac{k_0}{D_t^2} \sim t_0^3$, $\frac{k_0'}{D_t^2} \sim t_0^{2.5}$; Table 1). The tortuosity α_∞, which appears at the denominator of $f_{\nu t}$ is comparatively less influenced by the opening ratio t_o $\left(\alpha_\infty \sim \left(\frac{1}{t_0}\right)^{0.97}\right)$. This reflects the fact that the cellular structures were manufactured with large cell sizes ($D_t = 8\ mm$) and opening ratios $0.25 \le t_0 \le 0.6$, a choice which was largely influenced by the manufacturing constraints of the FDM technology. Another motivation which led us to choose relatively large cell sizes and opening ratios was related to the objective of promoting thermal relaxation effects θ_κ [$\theta_\kappa \sim \Re(\widetilde{k}')$, Eq. (23)] but on the other hand at minimal viscous dissipation effects θ_ν (which suggests increasing k_0 with a large t_0 at constant D_t, as discussed earlier).

Fig. 9. An image of 3D printed membrane structures for experimental tests.

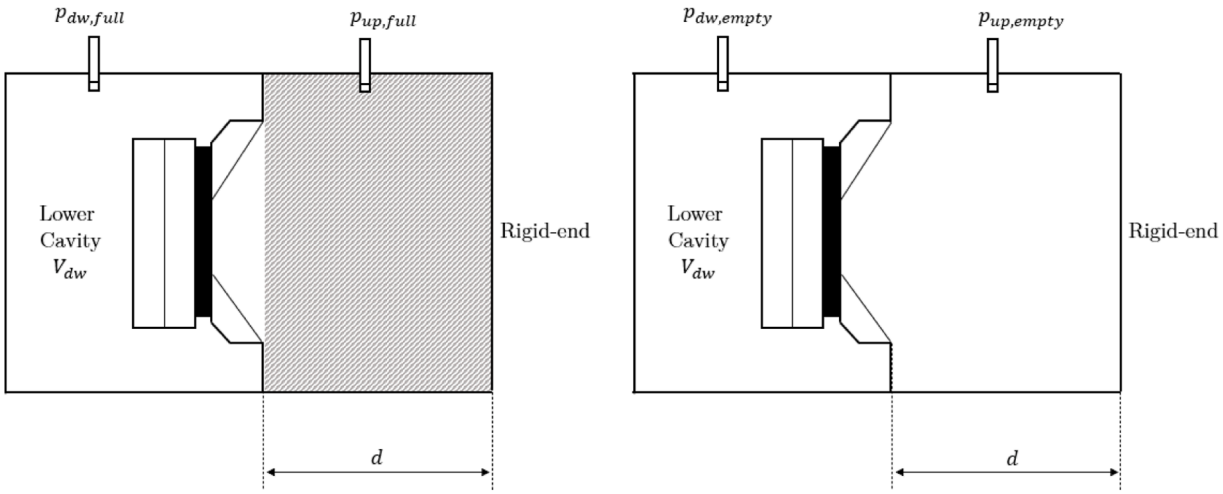

Fig. 10. Schematic illustration of the acoustic lumped element setup used to measure the complex bulk modulus for the full configuration (left panel), and the empty configuration (right panel).

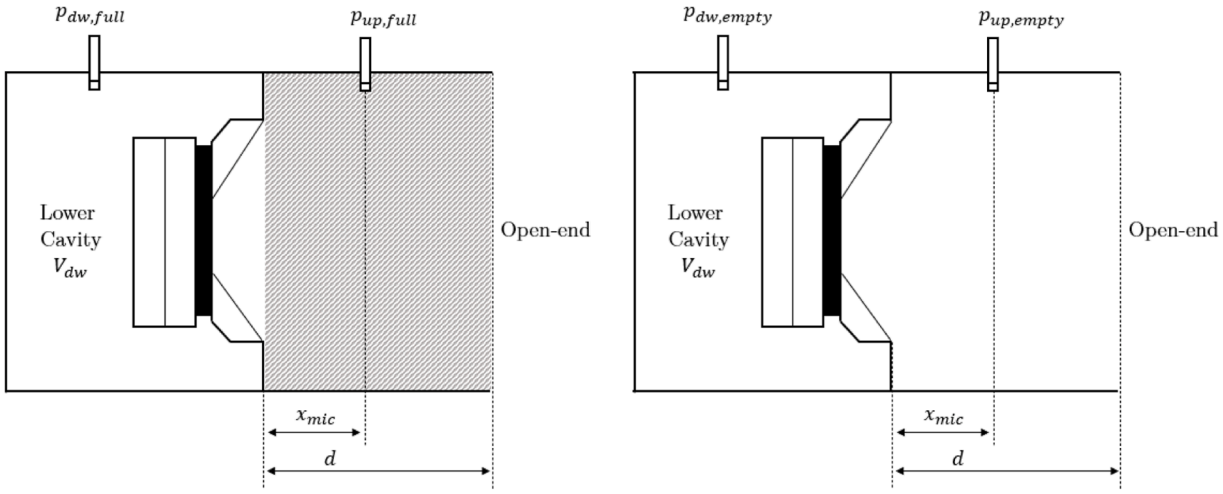

Fig. 11. Schematic illustration of the acoustic lumped element setup elaborated to experimentally evaluate the complex density from the *full* configuration (left panel) and the *empty* configuration (right panel).

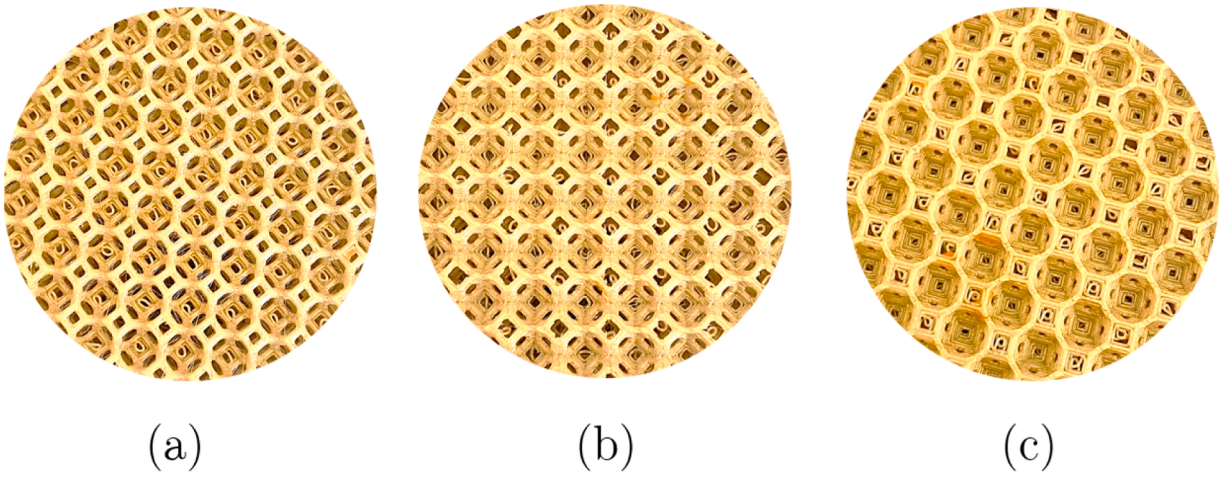

Fig. 12. Illustration of the three manufactured samples of three-dimensional cellular structures: (a) S3, $D_t = 8$ mm, $\xi = 0.8$ mm and $t_0 = 0.6$; (b) S2, $D_t = 8$ mm, $\xi = 0.8$ mm and $t_0 = 0.4$; (c) S1, $D_t = 8$ mm, $\xi = 0.8$ mm and $t_0 = 0.25$.

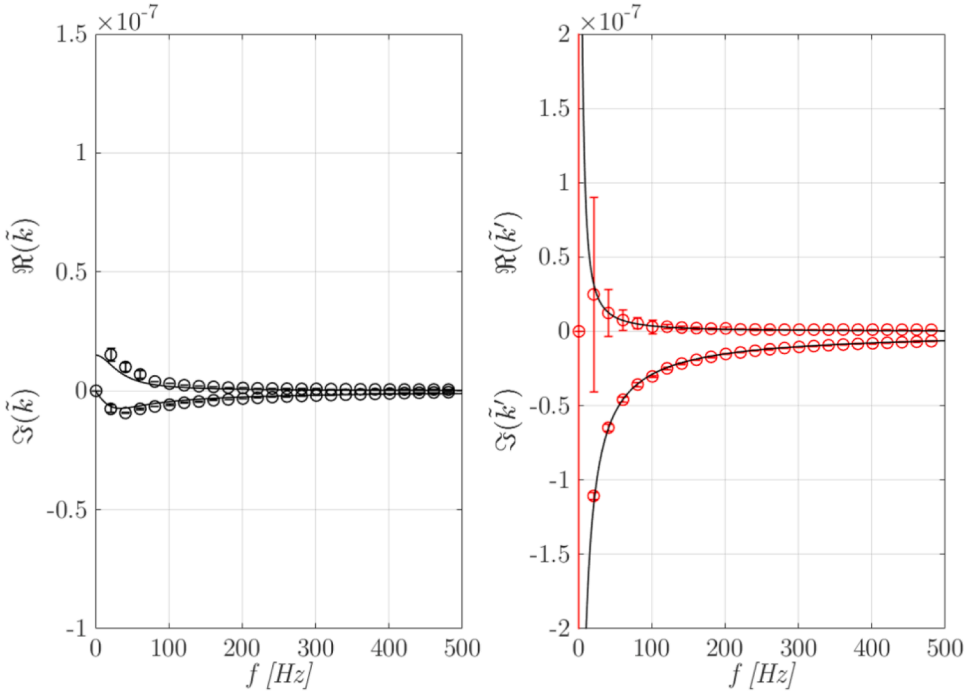

Fig. 13. Comparison between experimental results and the proposed modelling approach for the first manufactured cellular structure, S1. Circular points account for the mean values and the error bars stand for the measured standard deviations. The continuous black line corresponds to the real and imaginary parts of the frequency-dependent viscous permeability $\widetilde{k}$ (left panel) and thermal permeability $\widetilde{k}^{'}$ (right panel).

Finally, in Fig. 16 we compare directly the experimental and theoretical values of the thermal relaxation θ_κ and viscous dissipation θ_ν functions. The experimental data are generally in good agreement with the vertical shift towards lower viscous dissipation θ_ν as predicted by the model when increasing the opening ratio t_0 (from $t_0 = 0.25$ for S1, to $t_0 = 0.4$ for S2 and $t_0 = 0.6$ for S3). It is seen from Fig. 16.b that the measured viscous dissipation θ_ν is larger than the predicted one for the case of the third manufactured sample S3 characterized by the largest opening ratio ($t_0 = 0.6$). This behaviour is attributed to the presence of filaments, which are visible on the pictures of the manufactured cellular samples in Fig. 12 and are well known as an artefact of the additive manufacturing process [20]. Clearly, the effect of obstruction due to the presence of filaments becomes significant as we go to larger opening ratio. While the smallest windows of the manufactured sample S1 (Fig. 12.c) were apparently not affected by filaments, their presence is visible on the largest windows of all the manufactured samples (Fig. 12. a-c) which could contribute to lower the viscous permeability k_0 and increase the viscous dissipation θ_ν of the cellular structure S3 having the largest throats. We also note that, as the frequency increases, the experimental values of θ_ν starts to deviate from the model, in line with the previously mentioned limitations of the experimental method where the frequency validity range assumes that $|\widetilde{k}_n d| < 0.5$. By contrast, as predicted by the model, the thermal relaxation process is essentially controlled by the cell size D_t and not significantly influenced by the opening ratio t_0 (Fig. 5), which results in experimental values of the thermal relaxation θ_κ that are following the same trend (Fig. 16.a).

It is quite interesting to see that the key points of this research work are clearly validated by the experimental data provided throughout Fig. 16. Indeed, viscous dissipation θ_ν can be modulated and reduced by increasing the opening ratio t_0 while maintaining and controlling the thermal relaxation processes θ_κ to a significant level by playing on the cell size D_t, some trends fairly well described by our model and the corresponding proposed cellular structure.

8. Summary and conclusions

The main findings of this study are summarized in the following:

(1) A unified set of transport and diffusion calculations have been carried out on a family of realistic three-dimensional cellular structures; the tetrakaidecahedron unit cell parameterized with the cell size D_t, the opening ratio of the faces t_o and the thickness of the walls ξ.
(2) The model studied here provides an excellent candidate for additive manufacturing technologies and allows the modelling of viscous-thermal properties to be tested against experimental measurements.
(3) Correlations between the geometrical parameters of the cellular structure (D_t, t_o, ξ) and the transport properties characterizing visco-inertial and thermal effects (k_0 $k_0^{'}$, φ, Λ, $\Lambda^{'}$, α_∞) were also derived; they can be useful to avoid repeating our calculations.
(4) These structure-property relations were then used to study thermal and viscous exchanges in terms of frequency-dependent response functions, such as the dimensionless viscous dissipation θ_ν and thermal relaxation θ_k suggested by Swift et al. [3] in the context of thermoacoustic.
(5) The results shown in this study proved that the proposed cellular structure is an excellent way to promote thermal-relaxation processes while reducing viscous dissipation that could be detrimental to thermal-acoustic conversion; increase the cell size

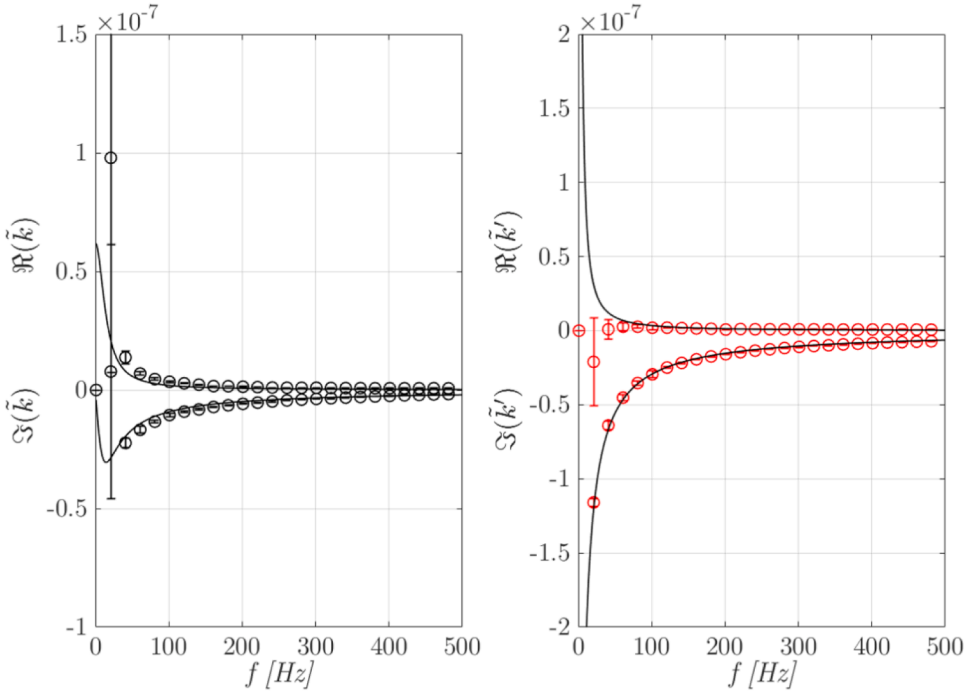

Fig. 14. Comparison between experimental results and the proposed modelling approach for the second manufactured cellular structure, S2. Circular points account for the mean values and the error bars stand for the measured standard deviations. The continuous black line corresponds to the real and imaginary parts of the frequency-dependent viscous permeability $\widetilde{k}$ (left panel) and thermal permeability $\widetilde{k}^{'}$ (right panel).

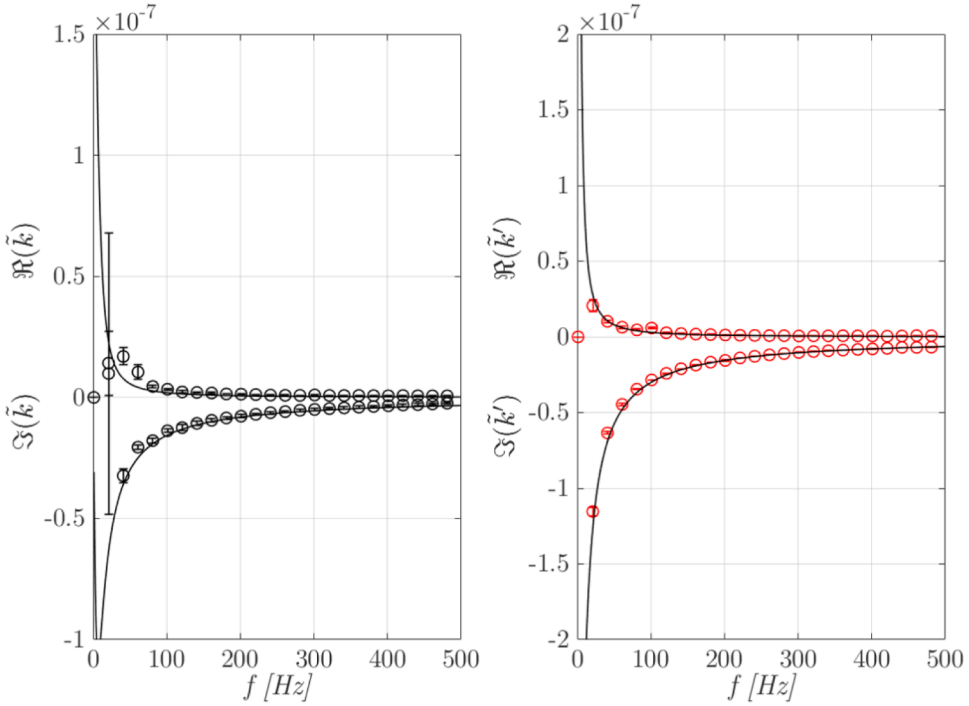

Fig. 15. Comparison between experimental results and the proposed modelling approach for the third manufactured cellular structure, S3. Circular points account for the mean values and the error bars stand for the measured standard deviations. The continuous black line corresponds to the real and imaginary parts of the frequency-dependent viscous permeability $\widetilde{k}$ (left panel) and thermal permeability $\widetilde{k}^{'}$ (right panel).

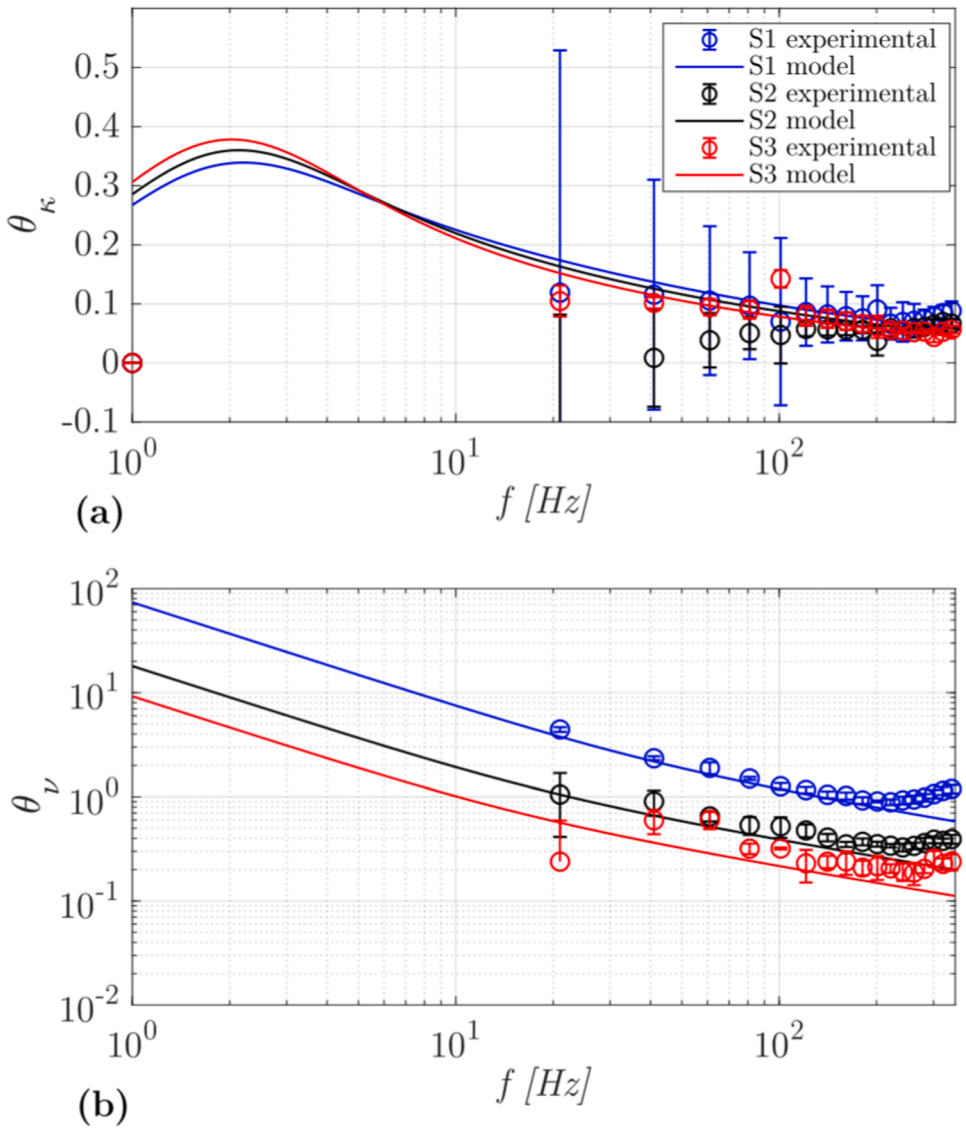

Fig. 16. Comparison between the experimental data and the model (a) for the thermal θ_κ and (b) viscous θ_ν relaxation parameters.

D_t and control the opening ratio t_o in a relatively independent manner.

(6) The model system studied here, while relatively simple, opens a new avenue in the thermal-acoustic domain, suggesting a way to significantly improve the overall energy efficiency of thermoacoustic engines when compared to conventional stacks.

CRediT authorship contribution statement

Elio Di Giulio: Writing – review & editing, Writing – original draft, Visualization, Software, Methodology, Investigation, Formal analysis, Data curation, Conceptualization. **Cong Truc Nguyen:** Software, Conceptualization. **Antonio Gloria:** Writing – review & editing, Visualization, Validation, Supervision. **Camille Perrot:** Writing – review & editing, Data curation, Conceptualization. **Raffaele Dragonetti:** Writing – review & editing, Validation, Supervision, Investigation, Formal analysis, Data curation, Conceptualization.

Declaration of competing interest

The authors declare that they have no known competing financial interests or personal relationships that could have appeared to influence the work reported in this paper.

Data availability

Data will be made available on request.

Acknoledgments

None

Supplementary materials

Supplementary material associated with this article can be found, in the online version, at doi:10.1016/j.ijheatmasstransfer.2024.126076.

Appendix A. JCAL model

Johnson et al. [11] provided a formulation of the dynamic viscous permeability (equivalent to the dynamic tortuosity) to describe the visco-inertial behaviour of a porous material. Three transport parameters, depending on the micro-geometrical features were introduced: the viscous and thermal characteristic lengths Λ and Λ', the high frequency limit of the tortuosity α_∞. These parameters influence the high frequency range of the viscous response function $\widetilde{k}_\nu$ (equivalent to $\widetilde{\rho}$), where the inertial forces dominate over the viscous ones. While the static viscous permeability k_0 (equivalent to the airflow resistivity $\sigma = \mu/k_0$) characterizes the low frequency behaviour where viscous frictions predominate. Champoux and Allard [45] contributed to the thermal characterization of a porous medium. Subsequently, Lafarge et al. [12] introduced a fundamental parameter to complete the low frequency description of the thermal behaviour: the static thermal permeability k_0', that together with the thermal characteristic length Λ' delineate the thermal response function $\widetilde{k}'$ (or $\widetilde{K}$) respectively in the low (isothermal) and high (adiabatic) frequency range. Further parameter is the porosity φ. The relations are reported in the following:

$$\widetilde{\rho} = \alpha_\infty \rho_m \left[1 + \frac{\mu\varphi}{i\omega\rho_m\alpha_\infty}\sqrt{1 + i\frac{4\alpha_\infty^2 k_0^2 \rho_m \omega}{\mu\Lambda^2\varphi^2}}\right], \tag{A.1}$$

$$\widetilde{K} = \frac{\gamma p_m}{\gamma - (\gamma-1)\left[1 - i\frac{\varphi\kappa}{k_0' c_p \rho_m \omega}\sqrt{1 + i\frac{4k_0'^2 c_p \rho_m \omega}{\kappa\Lambda'^2\varphi^2}}\right]}. \tag{A.2}$$

Appendix B. Relations between dynamic permeabilities, thermo-viscous functions, and complex density and bulk modulus.

This appendix details the mathematical relationships between several ways to describe a porous material's viscous and thermal properties. Dragonetti et al. [46] pointed out the link between the complex density $\widetilde{\rho}$ and bulk modulus $\widetilde{K}$ and the thermo-viscous functions f_ν and f_κ:

$$\widetilde{\rho} = \frac{\rho_m}{1 - f_\nu}, \tag{B.1}$$

$$\widetilde{K} = \frac{\gamma p_m}{1 + (\gamma-1) f_\kappa}. \tag{B.2}$$

The general solution of the linearized 1D momentum equation is expressed as

$$\frac{dp_1}{dx} = -\frac{i\omega\rho_m}{1 - f_\nu}\langle v_1\rangle. \tag{B.3}$$

By combining Eqs. (B.3) and (5), it follows that

$$\widetilde{k}(\omega) = \varphi\frac{\delta_\nu^2}{2i}(1 - f_\nu) = \varphi\frac{\delta_\nu^2}{2i}\frac{\rho_m}{\widetilde{\rho}}. \tag{B.4}$$

Furthermore, the linearized 1D energy equation yields

$$\langle T_1\rangle = \frac{p_1}{\rho_m c_p}(1 - f_\kappa). \tag{B.5}$$

This last equation, together, with Eq. (6), provides the link between the dynamic thermal permeability $\widetilde{k}$, the complex bulk modulus $\widetilde{K}$ and the dynamic thermal function f_κ:

$$\widetilde{k} = \varphi \frac{\delta_\kappa^2}{2i}(1 - f_\kappa) = \varphi \frac{\delta_\kappa^2}{2i} \frac{\gamma}{\gamma - 1}\left(1 - \frac{p_m}{\widetilde{K}}\right). \tag{B.6}$$

Therefore, Eqs. (B.1) and (B.2) can be combined with relationships (B.4) and (B.6) to predict the dynamic permeabilities $\widetilde{k}$ and $\widetilde{k}$.

In thermoacoustics, Swift [3] highlighted the importance of thermoviscous functions to assess the viscous losses and the thermal relaxation processes inside a porous material. The viscous $\dot{E}_\nu$ and thermal $\dot{E}_\kappa$ energy dissipations can be written as follow [2,3,47]

$$\frac{d\dot{E}_\nu}{dx} = -\frac{i\omega\rho_m}{A}\ \theta_\nu |U_1|^2, \tag{B.7}$$

$$\frac{d\dot{E}_\kappa}{dx} = -\frac{\gamma - 1}{\gamma p_m}\omega A\ \theta_\kappa |p_1|^2. \tag{B.8}$$

θ_ν and θ_κ represent respectively the microgeometrical viscous and thermal factors. They allow to consider the influence of the material's micro-geometry on the energy dissipation processes. In particular, they can be expressed as

$$\theta_\nu = \frac{\Im[-f_\nu]}{|1 - f_\nu|^2}, \tag{B.9}$$

$$\theta_\kappa = I[-f_\kappa]. \tag{B.10}$$

In Eqs. (22) and (23) for consistency in the treatment, these parameters are reported as function of the dynamic permeabilities, remembering Eqs. (B.4) and (B.6).

References

[1] A. Hossein Bashiri, A. Sangtarash, M. Zamani, The effect of the porous media on thermal management of lithium-ion battery pack; a comparative and numerical study, Therm. Sci. Engin. Progr 34 (2022) 101427, https://doi.org/10.1016/J.TSEP.2022.101427.

[2] J.F. Allard, N. Atalla, Propagation of Sound in Porous Media: Modelling Sound Absorbing Materials, John Wiley and Sons, 2009, https://doi.org/10.1002/9780470747339.

[3] G.W. Swift, Thermoacoustics : a Unifying Perspective For Some Engines and Refrigerators, Springer, 2018.

[4] G. Chen, L. Tang, Z. Yu, Modeling and analysis of a dual-acoustic-driver thermoacoustic heat pump, Therm. Sci. Engin. Progr 30 (2022) 101270, https://doi.org/10.1016/J.TSEP.2022.101270.

[5] L. Guo, D. Zhao, G. Yu, X. Dong, Numerical investigations on energy conversion performances in twin standing-wave thermoacoustic engines with various geometric and operational conditions, Therm. Sci. Engin. Progr 45 (2023) 102134, https://doi.org/10.1016/J.TSEP.2023.102134.

[6] V.V. Cherepanov, O.M. Alifanov, Modelling Techniques for ultra-porous heat-protective materials' spectral properties, Comput. Appl. Mathem 36 (2017) 281–300, https://doi.org/10.1007/S40314-015-0229-0/FIGURES/5.

[7] O.M. Alifanov, V.V. Cherepanov, A.G. Shchurik, R.A. Mironov, Calculation of characteristics of reticular materials based on a glassy carbon by its optical constants determined experimentally, J. Eng. Phys. Thermophys 93 (2020) 710–718, https://doi.org/10.1007/S10891-020-02170-Z/METRICS.

[8] P. Lotton, P. Blanc-Benon, M. Bruneau, V. Gusev, S. Duffourd, M. Mironov, G. Poignand, Transient temperature profile inside thermoacoustic refrigerators, Int. J. Heat. Mass. Transf 52 (2009) 4986–4996, https://doi.org/10.1016/J.IJHEATMASSTRANSFER.2009.03.075.

[9] N.M. Hariharan, P. Sivashanmugam, S. Kasthurirengan, Influence of operational and geometrical parameters on the performance of twin thermoacoustic prime mover, Int. J. Heat. Mass. Transf 64 (2013) 1183–1188, https://doi.org/10.1016/J.IJHEATMASSTRANSFER.2013.05.045.

[10] K. Kuzuu, S. Hasegawa, Effect of non-linear flow behavior on heat transfer in a thermoacoustic engine core, Int. J. Heat. Mass. Transf 108 (2017) 1591–1601, https://doi.org/10.1016/J.IJHEATMASSTRANSFER.2016.12.064.

[11] D.L. Johnson, J. Koplik, R. Dashen, Theory of dynamic permeability and tortuosity in fluid-saturated porous media, J. Fluid. Mech 176 (1987) 379–402, https://doi.org/10.1017/S0022112087000727.

[12] D. Lafarge, P. Lemarinier, J.F. Allard, V. Tarnow, Dynamic compressibility of air in porous structures at audible frequencies, J. Acoust. Soc. Am 102 (1998) (1995), https://doi.org/10.1121/1.419690.

[13] J.L. Auriault, C. Boutin, C. Geindreau, Homogenization of coupled phenomena in heterogenous media, homogenization of coupled phenomena in heterogenous media (2010). https://doi.org/10.1002/9780470612033.

[14] D. Westhoff, J. Skibinski, O. Šedivý, B. Wysocki, T. Wejrzanowski, V. Schmidt, Investigation of the relationship between morphology and permeability for open-cell foams using virtual materials testing, Mater. Des 147 (2018) 1–10, https://doi.org/10.1016/J.MATDES.2018.03.022.

[15] S. Torquato, Relationship between permeability and diffusion-controlled trapping constant of porous media, Phys. Rev. Lett 64 (1990) 2644, https://doi.org/10.1103/PhysRevLett.64.2644.

[16] N. Martys, E.J. Garboczi, Length scales relating the fluid permeability and electrical conductivity in random two-dimensional model porous media, Phys. Rev. B 46 (1992) 6080, https://doi.org/10.1103/PhysRevB.46.6080.

[17] E.T. Bird, A.E. Bowden, M.K. Seeley, D.T. Fullwood, Materials selection of flexible open-cell foams in energy absorption applications, Mater. Des 137 (2018) 414–421, https://doi.org/10.1016/J.MATDES.2017.10.054.

[18] A.S. Alsaman, H. Maher, M. Ghazy, E.S. Ali, A.A. Askalany, B. Baran Saha, 2D materials for adsorption desalination applications: a state of the art, Therm. Sci. Engin. Progr 49 (2024) 102455, https://doi.org/10.1016/J.TSEP.2024.102455.

[19] J. Costa-Baptista, E.R. Fotsing, J. Mardjono, D. Therriault, A. Ross, Design and fused filament fabrication of multilayered microchannels for subwavelength and broadband sound absorption, Addit. Manuf 55 (2022) 102777, https://doi.org/10.1016/J.ADDMA.2022.102777.

[20] T.G. Zieliński, K.C. Opiela, P. Pawłowski, N. Dauchez, T. Boutin, J. Kennedy, D. Trimble, H. Rice, B. Van Damme, G. Hannema, R. Wróbel, S. Kim, S. Ghaffari Mosanenzadeh, N.X. Fang, J. Yang, B. Briere de La Hosseraye, M.C.J. Hornikx, E. Salze, M.A. Galland, R. Boonen, A. Carvalho de Sousa, E. Deckers, M. Gaborit, J. P. Groby, Reproducibility of sound-absorbing periodic porous materials using additive manufacturing technologies: round robin study, Addit. Manuf 36 (2020) 101564, https://doi.org/10.1016/J.ADDMA.2020.101564.

[21] J. Boulvert, T. Cavalieri, J. Costa-Baptista, L. Schwan, V. Romero-García, G. Gabard, E.R. Fotsing, A. Ross, J. Mardjono, J.P. Groby, Optimally graded porous material for broadband perfect absorption of sound, J. Appl. Phys 126 (2019), https://doi.org/10.1063/1.5119715/595116.

[22] S. Deshmukh, H. Ronge, S. Ramamoorthy, Design of periodic foam structures for acoustic applications: concept, parametric study and experimental validation, Mater. Des 175 (2019) 107830, https://doi.org/10.1016/J.MATDES.2019.107830.

[23] V.H. Trinh, V. Langlois, J. Guilleminot, C. Perrot, Y. Khidas, O. Pitois, Tuning membrane content of sound absorbing cellular foams: fabrication, experimental evidence and multiscale numerical simulations, Mater. Des 162 (2019) 345–361, https://doi.org/10.1016/J.MATDES.2018.11.023.

[24] Z. Li, P. Wang, H. Zhao, C. Ao, Multi-objective optimization study of hydrothermal aging on NOx-assisted soot catalytic combustion and secondary pollution emission in regeneration of CeO2 catalytic diesel particulate filter, Therm. Sci. Engin. Progr 45 (2023) 102101, https://doi.org/10.1016/J.TSEP.2023.102101.

[25] M.R. Stinson, The propagation of plane sound waves in narrow and wide circular tubes, and generalization to uniform tubes of arbitrary cross-sectional shape, J. Acoust. Soc. Am 89 (1998) 550, https://doi.org/10.1121/1.400379.

[26] A. Di Meglio, E. Di Giulio, R. Dragonetti, N. Massarotti, A novel model for macroscopic simulation of oscillating heat and fluid flow in porous media, Int. J. Therm. Sci 181 (2022) 107758, https://doi.org/10.1016/J.IJTHERMALSCI.2022.107758.

[27] H.J. Rice, J. Kennedy, P. Göransson, L. Dowling, D. Trimble, Design of a Kelvin cell acoustic metamaterial, J. Sound. Vib 472 (2020) 115167, https://doi.org/10.1016/J.JSV.2019.115167.

[28] E. Di Giulio, F. Auriemma, M. Napolitano, R. Dragonetti, Acoustic and thermoacoustic properties of an additive manufactured lattice structure, J. Acoust. Soc. Am 149 (2021) 3878–3888, https://doi.org/10.1121/10.0005085.

[29] T.G. Zieliński, N. Dauchez, T. Boutin, M. Leturia, A. Wilkinson, F. Chevillotte, F. X. Bécot, R. Venegas, Taking advantage of a 3D printing imperfection in the development of sound-absorbing materials, Appl. Acoust 197 (2022) 108941, https://doi.org/10.1016/J.APACOUST.2022.108941.

[30] A. Ciochon, J. Kennedy, R. Leiba, L. Flanagan, M. Culleton, The impact of surface roughness on an additively manufactured acoustic material: an experimental and numerical investigation, J. Sound. Vib 546 (2023) 117434, https://doi.org/10.1016/J.JSV.2022.117434.
[31] W. Zhai, X. Yu, X. Song, L.Y.L. Ang, F. Cui, H.P. Lee, T. Li, Microstructure-based experimental and numerical investigations on the sound absorption property of open-cell metallic foams manufactured by a template replication technique, Mater. Des 137 (2018) 108–116, https://doi.org/10.1016/J.MATDES.2017.10.016.
[32] A. Di Meglio, E. Di Giulio, R. Dragonetti, N. Massarotti, Analysis of heat capacity ratio on porous media in oscillating flow, Int. J. Heat. Mass. Transf 179 (2021) 121724, https://doi.org/10.1016/J.IJHEATMASSTRANSFER.2021.121724.
[33] T.G. Zieliński, R. Venegas, C. Perrot, M. Červenka, F. Chevillotte, K. Attenborough, Benchmarks for microstructure-based modelling of sound absorbing rigid-frame porous media, J. Sound. Vib 483 (2020) 115441, https://doi.org/10.1016/J.JSV.2020.115441.
[34] C. Perrot, F. Chevillotte, R. Panneton, Dynamic viscous permeability of an open-cell aluminum foam: computations versus experiments, J. Appl. Phys 103 (2008), https://doi.org/10.1063/1.2829774.
[35] C. Perrot, R. Panneton, X. Olny, Computation of the dynamic thermal dissipation properties of porous media by Brownian motion simulation: application to an open-cell aluminum foam, J. Appl. Phys 102 (2007) 074917, https://doi.org/10.1063/1.2786899.
[36] R.J.S. Brown, Connection between formation factor for electrical resistivity and fluid-solid coupling factor in Biot's equations for acoustic waves in fluid-filled porous media, Geophysics 45 (1980) 1269–1275, https://doi.org/10.1190/1.1441123.
[37] M. Avellaneda, S. Torquato, Rigorous link between fluid permeability, electrical conductivity, and relaxation times for transport in porous media, Phys. Fluids A 3 (1998) 2529, https://doi.org/10.1063/1.858194.
[38] M. Firdaouss, J.L. Guermond, D. Lafarge, Some remarks on the acoustic parameters of sharp-edged porous media, Int. J. Eng. Sci 36 (1998) 1035–1046, https://doi.org/10.1016/S0020-7225(98)00002-0.
[39] O. Doutres, N. Atalla, K. Dong, Effect of the microstructure closed pore content on the acoustic behavior of polyurethane foams, J. Appl. Phys 110 (2011) 064901, https://doi.org/10.1063/1.3631021.
[40] V. Langlois, A. Kaddami, O. Pitois, C. Perrot, Acoustics of monodisperse open-cell foam: an experimental and numerical parametric study, J. Acoust. Soc. Am 148 (2020) 1767, https://doi.org/10.1121/10.0001995.
[41] V. Langlois, V.H. Trinh, C. Lusso, C. Perrot, X. Chateau, Y. Khidas, O. Pitois, Permeability of solid foam: effect of pore connections, Phys. Rev. E 97 (2018) 053111, https://doi.org/10.1103/PHYSREVE.97.053111/FIGURES/13/MEDIUM.
[42] M.Tan Hoang, C. Perrot, Solid films and transports in cellular foams, J. Appl. Phys 112 (2012) 054911, https://doi.org/10.1063/1.4751345.
[43] M. Napolitano, E. Di Giulio, F. Auriemma, R.A. Romano, R. Dragonetti, Low frequency acoustic method to measure the complex bulk modulus of porous materials, J. Acoust. Soc. Am 151 (2022) 1545–1556, https://doi.org/10.1121/10.0009767.
[44] E. Di Giulio, M. Napolitano, A. Di Meglio, R.A. Romano, R. Dragonetti, Low frequency acoustic method to measure the complex density of porous materials, J. Acoust. Soc. Am 152 (2022) 2220, https://doi.org/10.1121/10.0014762.
[45] Y. Champoux, J. Allard, Dynamic tortuosity and bulk modulus in air-saturated porous media, J. Appl. Phys 70 (1998) (1975), https://doi.org/10.1063/1.349482.
[46] R. Dragonetti, M. Napolitano, S. Di Filippo, R. Romano, Modeling energy conversion in a tortuous stack for thermoacostic applications, Appl. Therm. Eng 103 (2016) 233–242, https://doi.org/10.1016/J.APPLTHERMALENG.2016.04.076.
[47] P. Morse, K. Ingard, Theoretical acoustics, Princeton Press, 1986.